Journal of Solid State Chemistry 181 (2008) 2941–2952

Contents lists available at ScienceDirect

Journal of Solid State Chemistry

journal homepage: www.elsevier.com/locate/jssc

Phase and valence transitions in $Ba_2LnSn_xSb_{1-x}O_{6-\delta}$ (Ln = Pr and Tb)

Paul J. Saines [a], Brendan J. Kennedy [a,*], Margaret M. Elcombe [b], Hugh H. Harris [c], Ling-Yun Jang [d], Zhaoming Zhang [e]

[a] School of Chemistry, The University of Sydney, Sydney, New South Wales 2006, Australia
[b] Bragg Institute, ANSTO, Private Mail Bag 1, Menai, New South Wales 2234, Australia
[c] School of Chemistry and Physics, The University of Adelaide, Adelaide, South Australia 5005, Australia
[d] Research Division, National Synchrotron Radiation Research Center, Hsinchu 300, Taiwan
[e] Institute of Materials Engineering, ANSTO, Private Mail Bag 1, Menai, New South Wales 2234, Australia

ARTICLE INFO

Article history:
Received 14 May 2008
Received in revised form
8 July 2008
Accepted 10 July 2008
Available online 18 July 2008

Keywords:
Perovskite
Structural phase transition
Lanthanide valence state
XANES
Oxygen vacancies

ABSTRACT

Compounds in the double perovskites series $Ba_2LnSn_xSb_{1-x}O_{6-\delta}$ (Ln = Pr and Tb) have been synthesised and structurally characterised using synchrotron X-ray and neutron powder diffraction. It was found that the two end-members of the $Ba_2PrSn_xSb_{1-x}O_{6-\delta}$ series both adopt rhombohedral symmetry but the antimonate is a fully ordered double perovskite while the stannate has no *B*-site cation ordering. X-ray absorption near-edge structure (XANES) and near-infrared spectroscopy indicate that the Pr cations gradually change oxidation state from Pr^{3+} to Pr^{4+} with increasing x and that this is likely to be the cause of the loss of *B*-site ordering. Similarly, both Ba_2TbSbO_6 and $Ba_2TbSnO_{6-\delta}$ are cubic with *B*-site ordering present in the former but absent in the latter due to the oxidation state change of the Tb from Tb^{3+} to Tb^{4+}. Multiple linear regression analysis of the Pr and Tb L_{III}-edge XANES indicates that the rate of Ln^{3+} transforming to Ln^{4+} is such that there are no oxygen vacancies in $Ba_2PrSn_xSb_{1-x}O_{6-\delta}$ but in $Ba_2TbSn_xSb_{1-x}O_{6-\delta}$ there is a small amount of oxygen vacancies, with a maximum of $\delta \approx 0.05$ present.

1. Introduction

Materials with the perovskite-type structure are of significant interest to materials scientists due to the wide range of physical properties they exhibit [1]. One such property is the relatively high ionic and electronic conductivity exhibited by oxygen deficient perovskites [2–4]. High ionic conductivity usually takes the form of either high oxygen anion conductivity, as found in $La_{1-x}Sr_xGaO_{3-\delta}$ [5] or proton conductivity, such as in $BaCeO_{3-\delta}$ [6] or $Ba_2YSnO_{5.5}$ [7]. Perovskites with such properties are useful for application in solid oxide fuel cells, high-temperature oxygen separation, electrochemical reactors and oxygen sensors [2,8].

In general, it seems that high oxygen anion or proton conductivity is associated with a significant level of oxygen vacancies in the structure [2,4,8]. A higher level of oxygen vacancies leads to more vacant sites for oxygen ion diffusion. Alternatively, in the case of a proton conductor, a higher level of oxygen vacancies means that more water molecules can be accommodated into the structure in the form of hydroxide ions, which leads to more protons being present in the material [8]. Electronic conductivity is often associated with cations existing in two oxidation states [3]. In compounds with a cation that has the potential to exhibit mixed valencies, there is a clear relationship between the number of oxygen vacancies present and the proportion of the cation oxidised to the higher valence state. If the cation is readily oxidised, doping of the compound with a lower valence cation will lead to oxidation of the mixed valence cation rather than creating oxygen vacancies. Conversely, similar doping of a compound containing a mixed valence cation that has a preference for the lower valence state will result in the formation of more oxygen vacancies. The investigation of the degree of oxidation of mixed valence cations and the effect that this has on the amount of oxygen vacancies formed is of interest in perovskites due to the effect this will have on their conductivities.

In this work, compounds belonging to the series of double perovskites $Ba_2LnSn_xSb_{1-x}O_{6-\delta}$ (Ln = Pr and Tb) are explored with an emphasis on determining the valencies of the cations, particularly the lanthanides, and thereby examining the relative stability of oxygen vacancies in this series. This series of compounds was chosen because of their similarity to $Ba_2YSnO_{5.5}$, which is known to have good ionic, and particularly proton, conductivity [7]. Pr and Tb, however, are different from Y^{3+} as they can adopt either a trivalent or tetravalent oxidation state in oxide materials [9,10]. This presents the possibility that rather than having a similarly high level of oxygen vacancies as $Ba_2YSnO_{5.5}$,

* Corresponding author. Fax: +61 2 9351 3329.
E-mail address: B.Kennedy@chem.usyd.edu.au (B.J. Kennedy).

0022-4596/$ - see front matter Crown Copyright © 2008 Published by Elsevier Inc. All rights reserved.
doi:10.1016/j.jssc.2008.07.007

Pr^{4+} and/or Tb^{4+} may be present in the compounds $Ba_2PrSnO_{6-\delta}$ and $Ba_2TbSnO_{6-\delta}$, reducing the number of vacancies and therefore the conductivity. The doping of the Sn^{4+} site with Sb^{5+} allows a fine-tuning of the valence state of the lanthanide cations and/or the amount of oxygen vacancies present in the structure. Sb^{5+} was selected because of its similar ionic radius to Sn^{4+} (cf. 0.60 Å for Sb^{5+} and 0.69 Å for Sn^{4+} [11]) and the high chemical stability of the Ba_2LnSbO_6 series [12,13]. The structures of the antimonate end-member of the series, Ba_2PrSbO_6 and Ba_2TbSbO_6, have been well established as being $R\bar{3}$ rhombohedral (Glazer tilt system $a^-a^-a^-$ [14]) and $Fm\bar{3}m$ cubic ($a^0a^0a^0$), respectively [15,16]. The nature of the changes in the valency of *Ln* cations with increased Sn^{4+} doping, or alternatively the nature of the formation of oxygen vacancies, and the resultant effect this has on the structures adopted by these materials is of fundamental interest.

The two series $Ba_2PrSn_xSb_{1-x}O_{6-\delta}$ and $Ba_2TbSn_xSb_{1-x}O_{6-\delta}$ were synthesised by ceramic techniques and structurally characterised using a combination of synchrotron X-ray diffraction and, in selected cases, neutron diffraction both at and, where appropriate, above room temperature. Additionally, these compounds have also been examined using X-ray absorption near-edge structure (XANES) and UV–visible and near-infrared spectroscopies. These techniques were used as they are more accurate and precise methods than diffraction for examining the oxidation states of the cations in a compound and determining the extent of the oxygen deficiency.

2. Experimental

All starting materials were obtained from Aldrich Chemicals. The lanthanide oxides and barium carbonate were dried prior to use by heating overnight at 1000 and 100 °C, respectively. Samples of $Ba_2LnSn_xSb_{1-x}O_{6-\delta}$ (*Ln* = Pr or Tb and $x = 0, 0.1, 0.2, \ldots, 1$) were prepared from stoichiometric mixtures of $BaCO_3$, SnO_2, Sb_2O_3 and either Pr_6O_{11} or Tb_4O_7. The samples were finely ground as an acetone slurry and after being allowed to dry were heated at 800 °C for 24 h. After being reground, the samples were sequentially heated at 1000, 1100, 1150, 1200 and 1300 °C for periods of 24 h with samples being reground between each heating period. The reactions were monitored by powder X-ray diffraction using Cu*K*α radiation on a Shimadzu X-6000 Diffractometer to ensure that highly pure and crystalline samples were obtained. Where required these were then heated at 1350 °C for 48 h, 1400 °C for 24 h and 1450 °C for 24 h. One gram samples of the as synthesised $Ba_2PrSnO_{6-\delta}$ and $Ba_2TbSnO_{6-\delta}$ were heated under an atmosphere of 5% H_2 in Ar to examine what effect this had on the oxidation state of cations in the samples. This was done by heating these compounds to 800 °C at a rate of 5°/min and then immediately cooling them to room temperature. Additionally, a second sample of $Ba_2TbSnO_{6-\delta}$ was heated to 800 °C at the same rate and then held at that temperature for 24 h before cooling to room temperature.

Synchrotron X-ray diffraction patterns for the final samples were recorded on the Debye–Scherrer diffractometer at the Australian National Beamline Facility, beamline 20B at the Photon Factory, Tsukuba, Japan [17]. The samples were housed in 0.3 mm capillaries that were continuously rotated during measurement to reduce the effects of preferred orientation. Data were collected using three image plates as detectors covering the range of $5° < 2\theta < 125°$ with a step size of 0.01° and a wavelength of 0.80088(1), 0.80123(1), 0.80286(1) or 0.82606(1) Å. Variable temperature measurements, at temperatures of up to 800 °C, were carried out for selected samples using a custom built furnace with data collected over a range of $5° < 2\theta < 85°$.

Neutron powder diffraction data were collected for selected samples at room temperature using the high-resolution diffractometer, HRPD, at the HIFAR facility operated by the Australian Nuclear Science and Technology Organisation (ANSTO), Lucas Heights, Australia. A wavelength of either 1.4918(1) or 1.4924(1) Å was used to collect patterns over a range of $10° < 2\theta < 150°$ with a step size of 0.05° [18]. The samples were held in 12 mm vanadium cans that were continuously rotated during the measurements.

Refinements of the crystal structure were performed using the program RIETICA [19]. The diffraction peaks were described by a pseudo-Voigt function using a Howard asymmetry correction where necessary [19]. For neutron diffraction patterns, the background was calculated using a six-parameter polynomial while for the X-ray patterns the background was estimated from interpolation between up to 40 selected points. It should be noted that the estimated standard deviations of variables determined by the Rietveld refinement tend to underestimate the probable error in these values because they are based on random errors alone and do not include any systematic errors such as those in the wavelengths or models used [20,21].

Scanning electron microscopy (SEM) was used in combination with energy dispersive X-ray (EDX) analysis to examine the elemental composition of the phases present in selected samples. Samples were prepared as sintered pellets produced by applying 10 tonnes of pressure onto a 13 mm disc. The SEM and accompanying EDX analyses were carried out using a Phillips XL 30 scanning electron microscope, with a tungsten filament operating at 25 keV, a spot size setting of 5 and a working distance of 11 mm. The EDX analyses of elemental composition was performed in conjunction with the imaging process under the DX-4eDX ZAF operating system (version 3.3). Analysis was performed using the proprietary software in this system.

XANES experiments on both series were carried out at either beamline 20B at the Photon Factory in the case of the Tb-L_{III} edge, or at beamline 16A1 at the National Synchrotron Radiation Research Center (NSRRC), Hsinchu, Taiwan [22,23] in the case of the Pr, Sn and Sb *L*-edges. Measurements at beamline 20B were carried out in transmission mode using a channel cut Si(111) monochromator, which was detuned by 50% to reject higher harmonics. Samples were diluted in a BN matrix in a ratio of one part sample to five parts BN and placed between Kapton tape in a 1 mm thick sample holder capable of holding up to 12 samples. Spectra were collected by measuring the intensity of the X-rays at each energy using two ion chambers, one before and one after the sample. The incoming ion chamber was 31 cm long and filled with 30% N_2 in He while the transmitted ion chamber was 5 cm in length and filled with Ar. At beamline 16A1 spectra were measured in fluorescence mode with the sample dispersed on Kapton tape. X-rays were monochromated using a Si(111) double monochromator before reflecting off a higher-order harmonic light rejection mirror with spectra being measured using a Lytle detector. The energy of the spectra collected at beamline 16A1 were calibrated using the *K*-edge of a Cr foil while the spectra collected at beamline 20B were not calibrated due to problems with the Co foil selected for use as a reference. $Ln_2Sn_2O_7$ (*Ln* = Pr^{3+} and Tb^{3+}) and $BaLnO_3$ (*Ln* = Pr^{4+} and Tb^{4+}) were used as oxidation state standards for the trivalent and tetravalent oxidation states, respectively, as part of the analysis of the Pr and Tb L_{III}-edges. These compounds were synthesised in pure form using the methods of Kennedy et al. [24] for $Ln_2Sn_2O_7$ and Yoshimura et al. [25] and Hinatsu [26] for $BaLnO_3$. SnO and SnO_2 were used as standards for Sn^{2+} and Sn^{4+} and similarly Sb_2O_3 and Sb_2O_5 were employed as standards for Sb^{3+} and Sb^{5+}. These compounds are commercially available and were bought from Sigma–Aldrich.

XANES spectra were collected over the range of 7.295–7.809 keV and 5.764–6.740 keV for the Tb and Pr L_{III}-edges,

respectively, while, due to the Sn and Sb edges occurring in similar energy regions, the *L*-edges of both these cations were typically collected in a single scan over the energy range of 3.779–4.998 keV. Energy steps as small as 0.2 eV were employed near the absorption edges with a counting time of 1 and 2 s a step being used for data collected at beamline 20B and beamline 16A1, respectively. Subsequent to data collection, the spectra were normalised using either the BACKSUB procedure in EXAFSPAK [27] or SPLINE in XFIT [28]. Spectra normalised using BACKSUB and SPLINE were not directly compared with each other. Principal component, target transformation and multiple linear regression analyses of the XANES spectra were carried out using the PCA, TARGET and DATFIT programs in EXAFSPAK, respectively, to more thoroughly characterise and quantitatively examine the oxidation state of the lanthanide cations.

UV, visible and near-infrared spectra of the samples were measured using a Cary 5E UV–Vis–NIR spectrometer equipped with a diffuse reflectance attachment. Scans were taken between 200 and 2500 nm, using a data interval of 0.667 nm and a scanning rate of 200 nm/min. Polytetrafluoroethylene was used as the background for baseline scans with a standard correction being applied.

3. Results and discussion

The discussion of the characterisation of the $Ba_2LnSn_xSb_{1-x}O_{6-\delta}$ (Ln = Pr and Tb) series will consist of three sections. The first two of these will sequentially detail the structures adopted by the Pr and Tb series. The final section will examine the oxidation state of the cations present in these two series in more depth, using a combination of XANES, UV–visible and near-infrared spectroscopies. (*Note*: the oxidation states of Sn and Sb in $Ba_2LnSn_xSb_{1-x}O_{6-\delta}$ are assumed to be tetravalent and pentavalent, respectively, in Sections 3.1 and 3.2, which is subsequently confirmed by XANES in Section 3.3.)

3.1. Structures of $Ba_2PrSn_xSb_{1-x}O_{6-\delta}$

As determined by previous studies [15,16], Ba_2PrSbO_6 adopts the $R\bar{3}$ rhombohedral structure (tilt system $a^-a^-a^-$) with refinements of synchrotron X-ray diffraction patterns indicating that the cations are fully ordered in this compound (see Fig. 1). $Ba_2PrSnO_{6-\delta}$ was also found to be rhombohedral but did not exhibit the low angle *R*-point (100) and (111) Bragg reflections indicative of cation ordering (see Figs. 1 and S1 in the supplementary data). The Pr and Sn^{4+} cations in $Ba_2PrSnO_{6-\delta}$ are not ordered and it adopts the $R\bar{3}c$ ($a^-a^-a^-$) space group. A diffraction pattern of $Ba_2PrSnO_{6-\delta}$ obtained at 100 °C as part of this work did not contain any evidence for peak splitting showing that this compound undergoes a phase transition to the ideal $Pm\bar{3}m$ cubic structure below 100 °C.

The unit cell of $Ba_2PrSnO_{6-\delta}$ is considerably smaller than that of Ba_2PrSbO_6 (cf. a unit-cell volume of 153.68(6)–157.06(1) Å^3 for $Ba_2PrSnO_{6-\delta}$ and Ba_2PrSbO_6, respectively). Since Sn^{4+} has a larger ionic radius than Sb^{5+}, this suggests that some, or all, of the Pr cations in $Ba_2PrSnO_{6-\delta}$ may be tetravalent, compared with the antimonate where the Pr ions are trivalent. The difference between the ionic radius of Pr^{4+} and Pr^{3+} is larger than that between Sn^{4+} and Sb^{5+} (the ionic radius of Pr^{4+} and Pr^{3+} are 0.85 and 0.99 Å, respectively, [11]) and therefore the formation of Pr^{4+} in $BaPrSnO_{6-\delta}$ would explain the smaller unit-cell size. The loss of cation ordering is consistent with this hypothesis as the smaller charge and size (cf. a size difference of 0.16 Å for Pr^{4+} and Sn^{4+} to 0.39 Å for Pr^{3+} and Sb^{5+} [11]) difference between Pr^{4+} and Sn^{4+} would reduce the tendency of the *B*-site cations to order.

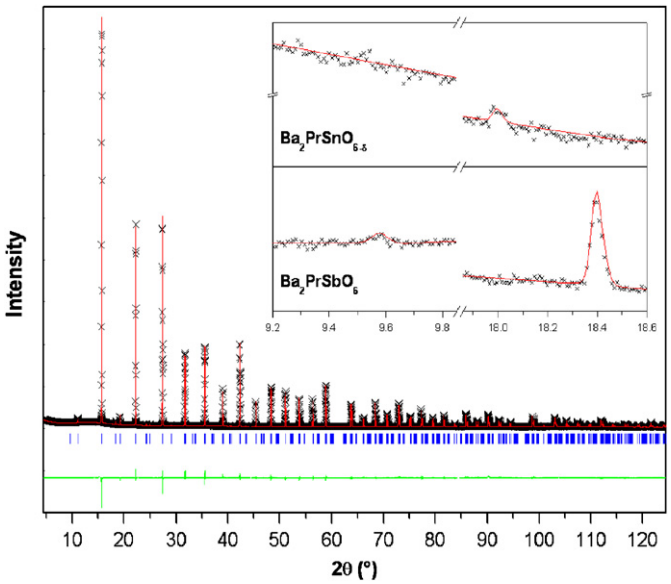

Fig. 1. Synchrotron X-ray diffraction pattern of Ba_2PrSbO_6 collected using a wavelength of 0.82606(1) Å. The crosses, upper and lower continuous lines represent the observed and calculated intensities and the difference between these respectively. The vertical markers show the positions of the allowed Bragg reflections. The inset shows the low-angle *R*-point super-lattice reflections for $Ba_2PrSnO_{6-\delta}$ and Ba_2PrSbO_6. The peak at ~18° is present in diffraction patterns of both samples as it is caused by both octahedral tilting and cation ordering while the lowest angle reflection is not present for $Ba_2PrSnO_{6-\delta}$ as it is caused by cation ordering alone, which is absent in this compound.

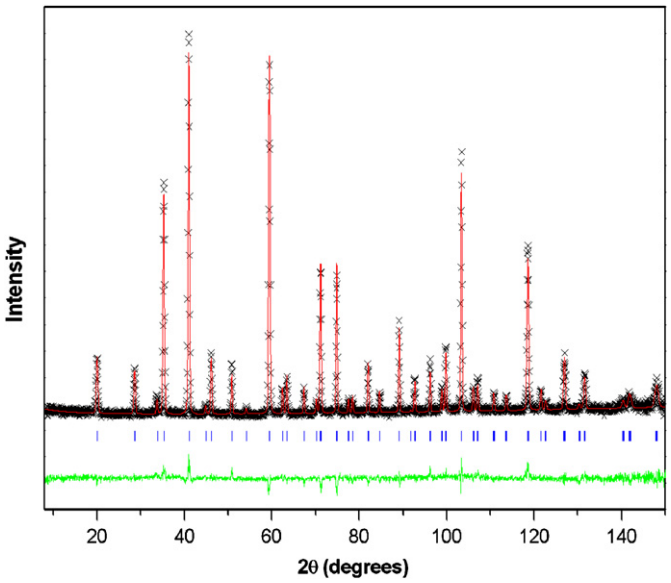

Fig. 2. Neutron diffraction pattern of $Ba_2PrSnO_{6-\delta}$ collected using a wavelength of 1.4924(1) Å, fitted with $R\bar{3}c$ symmetry. The format is the same as for Fig. 1.

The oxygen anion site in $Ba_2PrSnO_{6-\delta}$ refines as being 99.6(6) % occupied indicating that there is no evidence for oxygen vacancies in $Ba_2PrSnO_{6-\delta}$ and that effectively all the Pr in $Ba_2PrSnO_{6-\delta}$ is tetravalent (see Fig. 2 for an indication of the quality of the fit; R_p and R_{wp} are 6.7% and 8.1%, respectively). Similarly, a refinement against a neutron diffraction pattern of Ba_2PrSbO_6 yields an oxygen site occupancy of 101.5(6)% indicating that the Pr in the antimonate is all trivalent. Despite being slightly over 100% for consistency with the other refinements carried out in this work

Table 1
Lattice parameters and atomic positions for members of the series $Ba_2PrSn_xSb_{1-x}O_{6-\delta}$ determined using neutron diffraction

Compound	Ba_2PrSbO_6	$Ba_2PrSn_{0.4}Sb_{0.6}O_{6-\delta}$		$Ba_2PrSnO_{6-\delta}$
Space group	$R\bar{3}$	$I2/m$	$R\bar{3}c$	$R\bar{3}c$
a (Å)	6.0529(1)	6.0557(8)	6.0158(22)	6.0099(3)
b (Å)	$= a$	6.0393(6)	$= a$	$= a$
c (Å)	$= a$	8.5393(11)	$= a$	$= a$
α (deg)	60.147(2)	90	60.506(45)	60.056(4)
β (deg)	$= \alpha$	89.991(18)	$= \alpha$	$= \alpha$
γ (deg)	$= \alpha$	90	$= \alpha$	$= \alpha$
Ba	2c (x,x,x)	4i (x,0,z)	2a ($\frac{1}{4}$,$\frac{1}{4}$,$\frac{1}{4}$)	2a ($\frac{1}{4}$,$\frac{1}{4}$,$\frac{1}{4}$)
x	0.2505(4)	0.5016(22)	$\frac{1}{4}$	$\frac{1}{4}$
z	$= x$	0.2492(32)	$\frac{1}{4}$	$\frac{1}{4}$
B (Å^2)	0.66(3)	0.63(5)	2.76(56)	0.91(3)
Pr	1a (0,0,0)	2a (0,0,0)	2b (0,0,0)	2b (0,0,0)
B (Å^2)	0.66(7)	0.38(10)	0.68(42)	0.47(3)
B'	1b ($\frac{1}{2}$,$\frac{1}{2}$,$\frac{1}{2}$)	2d (0,0,$\frac{1}{2}$)	2b (0,0,0)	2b (0,0,0)
B (Å^2)	0.12(5)	0.17(9)	$=$ Pr B	$=$ Pr B
O1	6f (x,y,z)	4i (x,0,z)	6e (x,$\frac{1}{2}-x$,$\frac{1}{4}$)	6e (x,$\frac{1}{2}-x$,$\frac{1}{4}$)
x	0.7309(4)	−0.0350(20)	0.7839(26)	0.7270(2)
y	0.2390(3)	0	0.7161(26)	0.7730(2)
z	0.2988(2)	0.2591(20)	$\frac{1}{4}$	$\frac{1}{4}$
B (Å^2)	1.15(2)	0.57(12)	2.28(28)	1.60(2)
O 2		8j (x,y,z)		
x		0.2770(15)		
y		0.2521(20)		
z		0.0110(15)		
B (Å^2)		1.83(11)		
R_p (%)	6.2	4.4	6.7	
R_{wp} (%)	7.3	5.2	8.1	
χ^2	1.5	1.6	1.8	

In the $I2/m$ structure of $Ba_2PrSn_{0.4}Sb_{0.6}O_{6-\delta}$, the partial occupancy of the Pr site is fixed as 0.82 as determined from refinement of the synchrotron X-ray diffraction pattern with the remainder consisting of, in the appropriate stoichiometric ratio, Sn^{4+} and Sb^{5+}. The B' site is occupied in the opposite manner so as to maintain nominal stoichiometry.

Table 2
Bond distances and bond valence sums (BVS) for selected members of the series $Ba_2PrSn_xSb_{1-x}O_{6-\delta}$, as determined by neutron diffraction

x	Space group	Ba–O			Pr–O		B'–O	
		Bond length (Å)		BVS	Bond length (Å)	BVS	Bond length (Å)	BVS
0	$R\bar{3}$	3 × 2.8565(9) 3 × 3.029(5)	3 × 3.043(5) 3 × 3.2190(8)	1.69	6 × 2.312(2)	3.72	6 × 1.989(2)	5.28
0.4	$I2/m$	1 × 2.808(12) 2 × 2.882(10) 2 × 3.008(12) 2 × 3.0272(9)	2 × 3.047(11) 2 × 3.166(10) 1 × 3.250(12)	1.73 1.78	2 × 2.222(17) 4 × 2.268(13)	4.37	2 × 2.068(17) 4 × 2.018(20)	4.23 4.68
	$R\bar{3}c$	3 × 2.825(1) 6 × 3.015(15) 3 × 3.237(1)			6 × 2.145(22)	5.84	$=$ Pr–O	3.13 3.47
1	$R\bar{3}c$	3 × 2.8691(1) 6 × 3.008(1) 3 × 3.1459(1)		1.79	6 × 2.130(2)	6.08	$=$ Pr–O	3.27

The Pr^{3+}–O bond valence parameter was used for the calculation of the Pr–O BVS as the appropriate value for Pr^{4+} is not known. In the mixed Sn^{4+} and Sb^{5+} samples the BVS of Sn^{4+} is listed above that of Sb^{5+}.

the oxygen site occupancy of Ba_2PrSbO_6 was refined in the final model.

Refinements yield a Pr–O bond length of 2.312(2)Å in Ba_2PrSbO_6 compared with 2.130(2)Å in $Ba_2PrSnO_{6-\delta}$, consistent with a valency change from Pr^{3+} to Pr^{4+} (see Tables 1 and 2 for crystallographic details and selected bond distances, respectively). The Pr cations in the antimonate and tin compounds have a bond valence sum of 3.72 and 6.08 (based on the bond valence parameter for Pr^{3+}–O since the value for Pr^{4+} is unknown). These are very high values, particularly in the case of the Pr in $Ba_2PrSnO_{6-\delta}$, and are consistent with previous work in our group [15], which showed that such overbonding was present in all Ba_2LnSbO_6 compounds (Ln^{3+} = lanthanide). In contrast the Sn^{4+} cations in $Ba_2PrSnO_{6-\delta}$, which share the same site as the Pr cations, are significantly underbonded with a bond valence sum of 3.27. The apparent overbonding of the Pr^{4+} cations and the underbonding of the Sn^{4+} cations in $Ba_2PrSnO_{6-\delta}$ is, at least in part, a result of these cations sharing the same crystallographic site and may suggest that the local environment around these cations is distorted from the average environment determined by the Rietveld refinement. It should be mentioned that the displacement parameters of the oxygen anions in this structure were well fitted isotropically with no significant evidence for anisotropic behaviour as might be expected to be caused by such distortions.

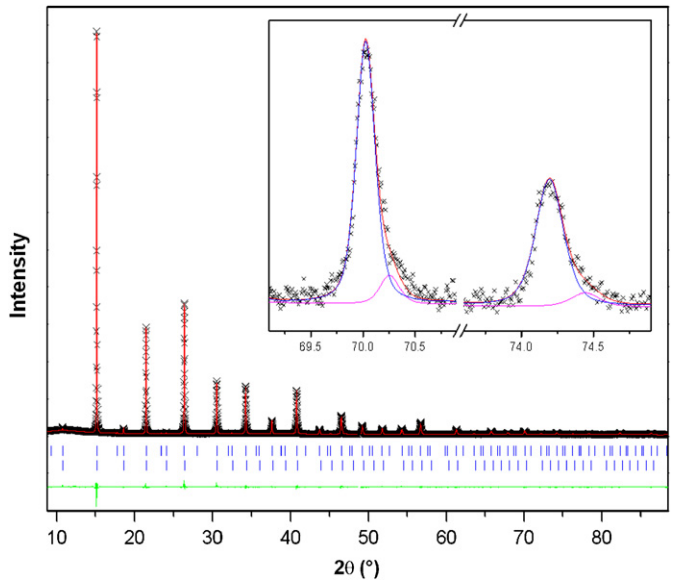

Fig. 3. Synchrotron X-ray diffraction pattern of $Ba_2PrSn_{0.3}Sb_{0.7}O_{6-\delta}$ at 760 °C collected using a wavelength of 0.80088(1) Å. The format is the same as for Fig. 1. The inset depicts the calculated intensities of the two cubic phases in the sample and the overall calculated intensity.

Having established that the two end-member oxides in the series $Ba_2PrSn_xSb_{1-x}O_{6-\delta}$, Ba_2PrSbO_6 and $Ba_2PrSnO_{6-\delta}$ adopt $R\bar{3}$ and $R\bar{3}c$ symmetry and most likely contain Pr in the trivalent and tetravalent state, respectively, the structures of the intermediate compounds were then investigated. The synchrotron X-ray diffraction patterns of the $x = 0.1$ and 0.2 samples had splitting and super-lattice reflections consistent with $R\bar{3}$ symmetry and were well fitted by models in this space group. The splitting of the X-ray diffraction patterns of the $x = 0.3$–0.9 samples were, however, significantly different from that of Ba_2PrSbO_6 (see Fig. S1). The diffraction pattern of the $x = 0.3$ sample was initially fitted using a model consisting of a single-phase $I2/m$ monoclinic ($a^-a^-c^0$) structure. Variable temperature synchrotron X-ray diffraction patterns, however, appeared to indicate that this structure was adopted up to 760 °C, the maximum temperature studied for this sample. This was an unexpected result and led to the re-examination of these patterns, which revealed that they were slightly better fitted by models consisting of two cubic phases (R_p and WR_p of 3.7% and 5.1% for the two-phase cubic model compared with 4.7% and 6.5% for the monoclinic model fitted to the 760 °C diffraction pattern). That $Ba_2PrSn_{0.3}Sb_{0.7}O_{6-\delta}$ consists of two cubic phases over the range of 100–760 °C confirms that the sample features some sort of cation segregation. Therefore, the room-temperature sample should also contain two phases. The fit of the two-phase model to the diffraction pattern collected at 760 °C suggests that the major phase makes up approximately 90% of the sample (see Fig. 3) explaining why the initial investigation of the sample at ambient temperature failed to detect the second minor phase. Subsequent fitting of the room-temperature X-ray diffraction patterns with a two-phase mixture of $I2/m$ monoclinic and $R\bar{3}c$ rhombohedral structures, the latter selected because it is the symmetry adopted by $Ba_2PrSnO_{6-\delta}$, provided a better fit than the $I2/m$ monoclinic structure alone (cf. an R_p and R_{Wp} of 3.2% and 4.5% for the two-phase $I2/m$ and $R\bar{3}c$ model to 4.6% and 6.0% for the single-phase monoclinic model).

Similar two-phase models consisting of $I2/m$ monoclinic and $R\bar{3}c$ rhombohedral structures provided the best fit to the synchrotron X-ray diffraction patterns of samples with $x = 0.4$–0.9. It should be noted that attempts to fit the room-temperature patterns of $x = 0.3$–0.9 compounds using two-phase mixtures of rhombohedral structures, as would be the case if these two-phase samples consisted of the structures belonging to the $x = 0$ and 1.0 end-members, were unsuccessful as they did not account for certain peak broadening that was consistent with the splitting of the monoclinic phase (see Fig. S1). Variable temperature X-ray diffraction patterns of $Ba_2PrSn_{0.4}Sb_{0.6}O_{6-\delta}$ indicate that, similar to $Ba_2PrSn_{0.3}Nb_{0.7}O_{6-\delta}$, it remains a two-phase mixture up to the maximum temperature examined, in this case 800 °C, where it is well fit by two cubic phases. Models fitted to the synchrotron X-ray diffraction patterns from the series $Ba_2PrSn_xSb_{1-x}O_{6-\delta}$ indicate that the degree of *B*-site cation disorder in the double perovskite $R\bar{3}$ and $I2/m$ phases generally increases with increasing x.

The large two-phase region in this series and its persistence to very high temperature, as seen in $Ba_2PrSn_{0.3}Sb_{0.7}O_{6-\delta}$ and $Ba_2PrSn_{0.4}Sb_{0.6}O_{6-\delta}$, would appear to indicate that these two structures form as a result of segregation into two phases with different chemical composition. A combination of EDX analysis and backscattered electron images collected using SEM was then used to investigate if any cation segregation was present. There were no significantly contrasting regions in the backscattered images (see Fig. S2). EDX analysis did not find any significant variation in the cation concentrations in the regions studied across the sample, hence confirming their homogeneity over the spatial range that can be resolved by these techniques. It should, however, be noted that because tin and antimony have similar atomic numbers (50 and 51, respectively) they have X-ray emission spectra that overlap to a significant extent, giving rise to some correlation between the amount of Sn^{4+} and Sb^{5+} determined at each point by EDX. It is possible that there may be some small amount of Sn^{4+} and Sb^{5+} segregation between the two phases that is not large enough to be detectable because of this emission spectra overlap.

It is possible that the failure of SEM and EDX analysis to reveal any significant cation segregation in the two-phase $Ba_2PrSn_xSb_{1-x}O_{6-\delta}$ samples may be a result of it occurring over a spatial resolution smaller than can be probed by using the available instrumentation. Alternatively, a different cause of the phase segregation may be required. Examination of the lattice parameters of the monoclinic and rhombohedral phases shows that the unit cell of the monoclinic phase is significantly larger than that of the rhombohedral phase in each sample (see Fig. 4). Preferential concentration of the Pr^{3+} into the monoclinic phase and Pr^{4+} in the rhombohedral phase could account for this given the significant size difference between Pr^{3+} and Pr^{4+}. Segregation of different oxidation states of the same element would not be detectable by EDX analysis explaining why this technique suggests the samples to be chemically homogeneous. Refinement of the neutron diffraction pattern of $Ba_2PrSn_{0.4}Sb_{0.6}O_{6-\delta}$ reveals that the average bond length of the Pr site in the monoclinic phase is much longer than the mixed Pr/Sn/Sb site in the rhombohedral phase (see Table 2). Furthermore, the amount of the rhombohedral phase present relative to the monoclinic phase increases with increasing x, as the Pr^{4+} rich phase would be expected to as the total amount of Pr^{4+} in the sample increases. Both of these observations are consistent with the above hypothesis.

3.2. *Structures of $Ba_2TbSn_xSb_{1-x}O_{6-\delta}$*

Consistent with previous work by our group [15], a synchrotron X-ray diffraction pattern of Ba_2TbSbO_6 reveals that it adopts a fully ordered *B*-site cation structure belonging to the untilted $Fm\bar{3}m$ cubic symmetry. $Ba_2TbSnO_{6-\delta}$ is also found to be metrically cubic but lacks the *R*-point super-lattice reflections which, in the untilted cubic structure, indicate the presence of *B*-site cation

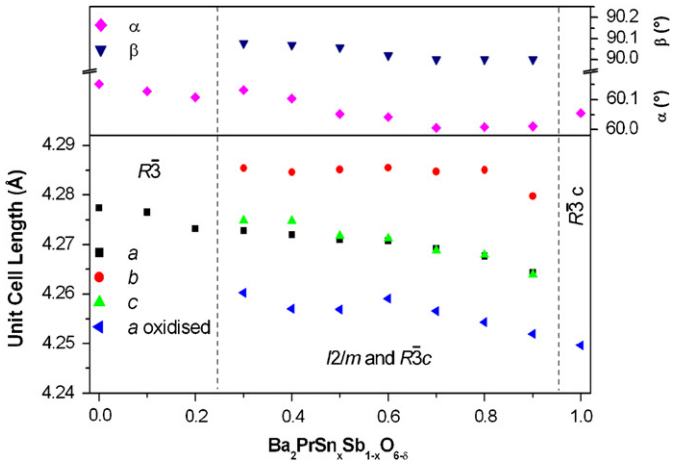

Fig. 4. Lattice parameters for compounds in the series $Ba_2PrSn_xSb_{1-x}O_{6-\delta}$ (“a oxidised” corresponds to the rhombohedral phase considered to contain mainly oxidised Pr^{4+}). Unit-cell lengths have been reduced to the size of the primitive cubic perovskite for ease of comparison.

Table 3
Lattice parameters, atomic positions and displacement parameters for compounds in the series $Ba_2TbSn_xSb_{1-x}O_{6-\delta}$ as determined using neutron diffraction

Compound	Ba_2TbSbO_6	$Ba_2TbSn_{0.8}Sb_{0.2}O_{6-\delta}$	$Ba_2TbSnO_{6-\delta}$
Space group	$Fm\bar{3}m$	$Fm\bar{3}m$	$Pm\bar{3}m$
a (Å)	8.4494(2)	8.4097(2)	4.19925(7)
Ba	8*c* ($\frac{1}{4},\frac{1}{4},\frac{1}{4}$)	8*c* ($\frac{1}{4},\frac{1}{4},\frac{1}{4}$)	1*b* ($\frac{1}{2},\frac{1}{2},\frac{1}{2}$)
B (Å^2)	0.49(2)	0.64(3)	0.57(2)
Tb	4*a* (0,0,0)	4*a* (0,0,0)	1*a* (0,0,0)
B (Å^2)	0.32(4)	0.40(3)	0.32(1)
B'	4*b* ($\frac{1}{2},\frac{1}{2},\frac{1}{2}$)	4*b* ($\frac{1}{2},\frac{1}{2},\frac{1}{2}$)	1*a* (0,0,0)
B (Å^2)	0.20(4)	0.40(3)	= Tb B
O1	24*e* (*x*,0,0)	24*e* (*x*,0,0)	3*d* ($\frac{1}{2}$, 0, 0)
x	0.2657(1)	0.2534(5)	$\frac{1}{2}$
B (Å^2)	0.82(2)	1.00(2)	0.83(2)
Occupancy	0.995(5)	0.976(6)	0.986(7)
R_p (%)	5.9	6.1	5.6
R_{Wp} (%)	7.1	7.3	6.8
χ^2	1.8	1.4	1.6

In the case of the partially disordered $Ba_2TbSn_{0.8}Sb_{0.2}O_{6-\delta}$ structure, the Tb site refines as containing 56(4) % Tb cations.

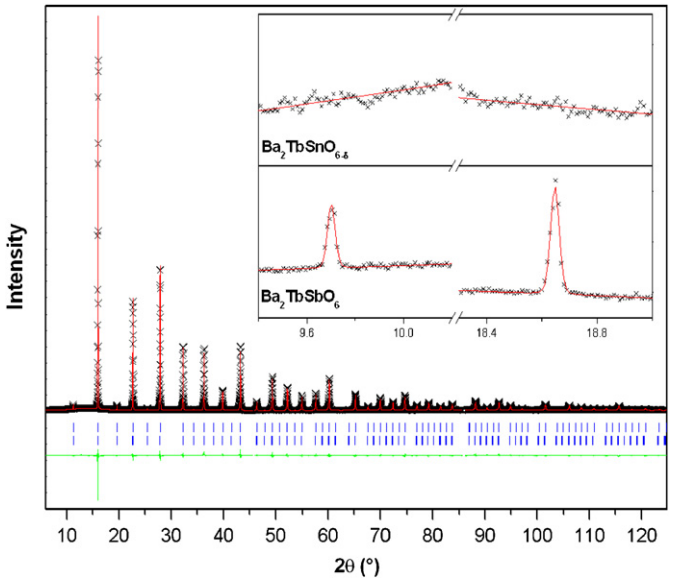

Fig. 5. Synchrotron X-ray diffraction pattern of $Ba_2TbSnO_{6-\delta}$ collected using a wavelength of 0.82606(1) Å. The format is the same as in Fig. 1. The inset displays the two lowest angle *R*-point super-lattice reflections of Ba_2TbSbO_6 and the same region of the pattern of $Ba_2TbSnO_{6-\delta}$.

ordering (see Figs. 5 and S3). As in $Ba_2PrSnO_{6-\delta}$, the Tb and Sn^{4+} cations in $Ba_2TbSnO_{6-\delta}$ share the same site in a $Pm\bar{3}m$ cubic perovskite structure.

The peaks in both the synchrotron X-ray and neutron diffraction patterns of $Ba_2TbSnO_{6-\delta}$ are notably asymmetric, especially in the higher-resolution X-ray diffraction data, with this asymmetry increasing at higher angles (see Fig. S3). This asymmetry is not consistent with subtle unresolved splitting of a lower symmetry structure. Rather it is similar to the asymmetry noted in the peak shapes of the related compound Ba_2InNbO_6 by Ting et al. [29], which adopts the $Fm\bar{3}m$ cubic structure with a high degree of *B*-site cation disorder. Ting et al. postulated that this unusual peak shape is caused by strain induced by twinning and stacking faults resulting from disorder of the *B*-site cations. Since the *B*-site cations in $Ba_2TbSnO_{6-\delta}$ are disordered it is likely that the peak shape observed in this compound is caused by a similar effect.

Ting et al. [29] included a second *P*4/*mmm* “phase” in their model to account for the observed peak asymmetry and using a similar model to fit the synchrotron X-ray and neutron diffraction patterns of $Ba_2TbSnO_{6-\delta}$ results in a significant improvement in the quality of the fits, this can be clearly seen by the large improvement of R_p and R_{Wp} factors from 9.3% and 13.4% to 4.9% and 6.2% for a fit to the synchrotron X-ray diffraction data and a significant improvement in the quality of the fit to the neutron diffraction pattern (R_p and WR_p of 6.2% and 7.7% cf. to 5.6% and 6.8%). While it is also possible that the asymmetric peak shape of the $Ba_2TbSnO_{6-\delta}$ sample may be caused by the sample containing a small amount of another perovskite impurity this asymmetry does not resolve into split peaks even at high angles in the synchrotron X-ray diffraction pattern. Additionally, refinement of the peak shape parameters of the second phase against the synchrotron X-ray diffraction pattern yields a very broad peak shape rather than the sharp features that would be expected for a genuine perovskite impurity “phase”. This indicates that the peak asymmetry is a result of strain induced in the sample by *B*-site cation disorder and the related presence of stacking faults and not by compositional differences in the samples.

The smaller unit-cell volume of $Ba_2TbSnO_{6-\delta}$ compared with Ba_2TbSbO_6 (cf. 73.8778(7) to 75.3947(8) Å^3 for $Ba_2TbSnO_{6-\delta}$ and Ba_2TbSbO_6, respectively, when reduced to the size of the primitive cubic unit cell) and the lack of cation order in $Ba_2TbSnO_{6-\delta}$ suggest that, as for $Ba_2PrSnO_{6-\delta}$ Tb is present as Tb^{3+} in Ba_2TbSbO_6 and Tb^{4+} in $Ba_2TbSnO_{6-\delta}$. The change in bond lengths between Ba_2TbSbO_6 and $Ba_2TbSnO_{6-\delta}$ is also consistent with an oxidation state change from Tb^{3+} to Tb^{4+}. Refinement of models against neutron diffraction patterns show that the Tb–O bond length shortens from 2.2449(8) Å in Ba_2TbSbO_6 to 2.09963(4) Å in $Ba_2TbSnO_{6-\delta}$, which is a change of approximately 0.15 Å (see Tables 3 and 4 for crystallographic information and bond lengths, respectively). This is very close to the 0.16 Å difference between the ionic radii of Tb^{3+} and Tb^{4+}, which are 0.92 and 0.76 Å, respectively, [11]. As in the Pr compounds, Tb is over-bonded in both structures with a bond valence sum of 3.53 and 5.23 for Ba_2TbSbO_6 and $Ba_2TbSnO_{6-\delta}$. The bond valence sums were determined using the parameter for a Tb^{3+}–O bond since the appropriate parameter for Tb^{4+} is unknown.

Refinements from neutron diffraction patterns of Ba_2TbSbO_6 and $Ba_2TbSnO_{6-\delta}$ have oxygen anion sites that are 99.5(5)% and 98.6(7)% of full occupancy. This is consistent with Ba_2TbSbO_6

Table 4
Bond lengths and bond valence sums (BVS) for selected compounds in the $Ba_2TbSn_xSb_{1-x}O_{6-\delta}$ series determined from refinements using neutron diffraction patterns

X	Ba–O		Tb–O		B'–O	
	Bond length (Å)	BVS	Bond length (Å)	BVS	Bond length (Å)	BVS
0	$12 \times 2.9903(1)$	1.81	$6 \times 2.2449(8)$	3.53	$6 \times 1.9798(8)$	5.42
0.8	$12 \times 2.9734(1)$	1.89	$6 \times 2.131(4)$	4.80	$6 \times 2.073(4)$	3.81 4.21
1.0	$12 \times 2.9693(1)$	1.91	$6 \times 2.0996(1)$	5.23	$=$ Tb–O	3.55

The BVS for Tb is based on the Tb^{3+}–O parameter since the appropriate value for Tb^{4+} is not known. In the case of the mixed Sn^{4+} and Sb^{5+} structure the BVS for Sn^{4+} is listed above that of Sb^{5+}.

being stoichiometric in regards to oxygen content indicating that the Tb in this compound is all in the trivalent state. On the other hand, the oxygen occupancy found for $Ba_2TbSnO_{6-\delta}$ equates to a stoichiometry of $Ba_2TbSnO_{5.92(4)}$. This is equivalent to 83(8)% of the Tb in this compound being tetravalent with the remainder being trivalent. This is slightly lower than the valency of Pr in $Ba_2PrSnO_{6-\delta}$, where neutron diffraction indicated that effectively all the Pr (95(8)%) is tetravalent. Determination of oxygen occupancy by the Rietveld refinement against neutron diffraction patterns, however, suffers from the strong cross-correlation between the occupancy and displacement parameters of a site particularly in data that do not cover an extensive range of *d*-space. Therefore, an oxygen occupancy that is lower than the true value can be compensated for in the refinement by a lower atomic displacement parameter. To determine a more accurate estimate of the oxidation state of cations, and thereby the level of oxygen vacancies, in compounds in the series $Ba_2LnSn_xSb_{1-x}O_{6-\delta}$ (Ln = Pr and Tb), samples were probed by XANES, UV–visible and near-infrared spectroscopies as discussed in the following section.

In brief both Ba_2TbSbO_6 and $Ba_2TbSnO_{6-\delta}$ are cubic and Tb exists primarily as Tb^{3+} in the former and Tb^{4+} in the latter, causing the loss of *B*-site cation ordering and a change of symmetry from $Fm\bar{3}m$ to $Pm\bar{3}m$. Having established this, the series $Ba_2TbSn_xSb_{1-x}O_{6-\delta}$ was investigated using synchrotron X-ray and neutron diffraction to determine the point at which the transition occurs. Refinements reveal a gradual increase in *B*-site disorder with increased tin doping and that the transition occurs between $x = 0.8$ and 0.9. This is accompanied by a gradual shortening of the Tb–O bonds and a lengthening of the Sn/Sb–O bonds such that the Tb–O and Sn/Sb–O bond lengths in $Ba_2TbSn_{0.8}Sb_{0.2}O_{6-\delta}$, the last ordered structure before the symmetry changes, are very similar (see Table 4). The gradual change in *B*-site bond distances with increasing x suggests that the oxidation state changes steadily from Tb^{3+} to Tb^{4+} across the series rather than suddenly at a specific composition. This is consistent with the gradual decrease in unit-cell length and unit-cell volume observed with increasing x (see Fig. 6). It should be mentioned that these refinements are carried out with the constraint that any disordering of the *B*-site cations involves both Sn^{4+} and Sb^{5+} replacing Tb in a ratio consistent with the composition of the compound (i.e., a partial occupancy of 0.2 of the Sn^{4+} and Sb^{5+} cation on the Tb site in $Ba_2TbSn_{0.6}Sb_{0.4}O_{6-\delta}$ consists of a partial occupancy of 0.12 and 0.08 of Sn^{4+} and Sb^{5+}). This constraint is necessary because Sn^{4+} and Sb^{5+} have similar neutron scattering lengths (cf. a coherent neutron scattering length of 6.225(2) fm for Sn^{4+} to 5.57(3) fm for Sb^{5+} [30]) and the same number of electrons, leading to very weak or no contrast in neutron and X-ray diffraction.

The peak asymmetry observed in $Ba_2TbSnO_{6-\delta}$ is noticeable in a number of other compounds in this series. In compositions

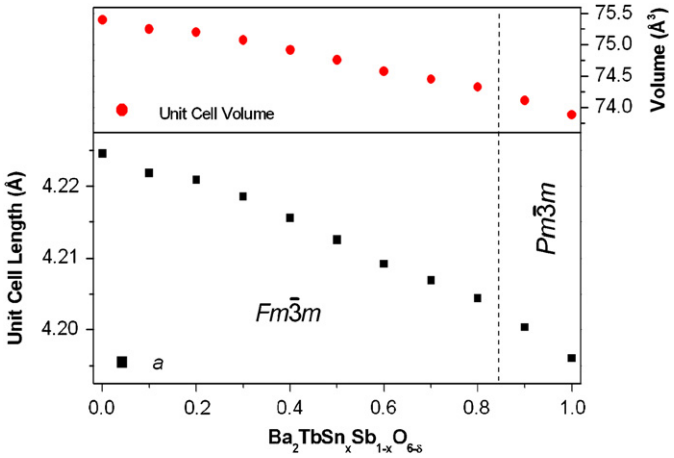

Fig. 6. Reduced unit-cell length and unit-cell volume of members in the series $Ba_2TbSn_xSb_{1-x}O_{6-\delta}$.

where $x = 0.2$–0.4 the longer sloping tail of the asymmetric peaks is on the higher angle (lower *d*-spacing) side of the peak, while in $x = 0.8$–1.0 the longer tail is on the lower angle (higher *d*-spacing) side of the peak) (see Fig. S3). Consequently in the $x = 0.2$–0.4 range of compositions, the lattice parameters of the secondary "phase" are smaller than those of the main phase, while in the 0.8–1.0 range they are larger. The asymmetric peak shape found in these samples may provide an insight into the stresses present in these materials. Where the lattice parameters of the secondary "phase" are smaller than that of the main phase the stress is most likely compressive while tensile stress is suggested to be dominant where the secondary "phase" has larger lattice parameters. In the $x = 0.5$–0.7 samples, where there is no obvious peak asymmetry, a comparable mix of the two appears to be present. Why this should be the case is not obvious, although it may be related to the changing quantities of the four different sized *B*-site cations, Tb^{3+}, Tb^{4+}, Sn^{4+} and Sb^{5+}, throughout the series. The existence of stress in these complex oxides is not surprising either for the same reason. Suitable thermal treatment or heating under a different environment may reduce the stress in these materials and this would be of interest for further study.

3.3. Analysis of oxygen vacancies and oxidation states of cations in $Ba_2LnSn_xSb_{1-x}O_{6-\delta}$

The structural analysis of compounds in the series $Ba_2LnSn_xSb_{1-x}O_{6-\delta}$ (Ln = Pr and Tb) provided a strong indication that as x increases the lanthanide cations change from the trivalent to tetravalent states reducing or eliminating the need for oxygen vacancies to form. There are, however, more suitable techniques for accurately determining the oxidation states of the cations in a material. Therefore in the work presented in this section, the oxidation states, and thereby amount of oxygen vacancies, in the series $Ba_2LnSn_xSb_{1-x}O_{6-\delta}$ have been analysed using UV–visible and near-infrared spectroscopy and XANES. Both of these techniques have their strengths with UV–visible and near-infrared spectroscopy being easily accessible, quick and easy to use while XANES offers the potential to quantitatively probe the oxidation state of cations in a material.

The 1200–1900 nm region of the near-infrared spectra of $Ba_2PrSn_xSb_{1-x}O_{6-\delta}$ reveals that the many sharp peaks present in Ba_2PrSbO_6 are replaced in the spectra of $Ba_2PrSnO_{6-\delta}$ by fewer, broader and more intense features (see Fig. 7). These features correspond to low lying transitions between the 4*f* orbitals, and the sharp features in the Ba_2PrSbO_6 spectra and the broad features

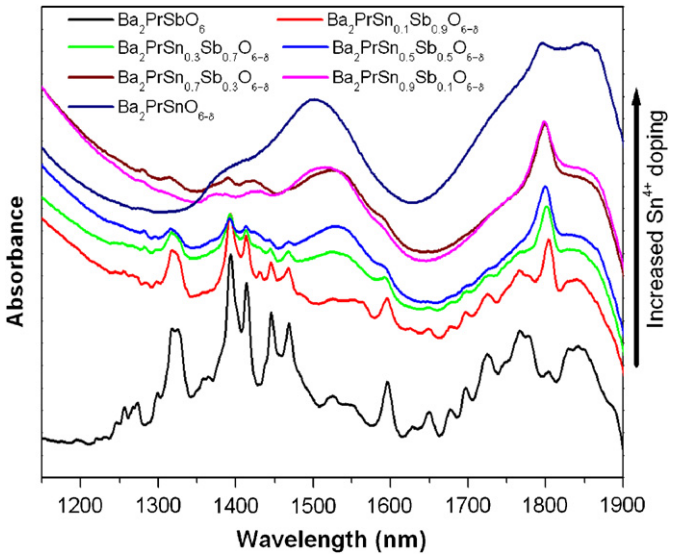

Fig. 7. Near-infrared spectra of selected compounds in the series $Ba_2PrSn_xSb_{1-x}O_{6-\delta}$ in the region 1150–1900 nm.

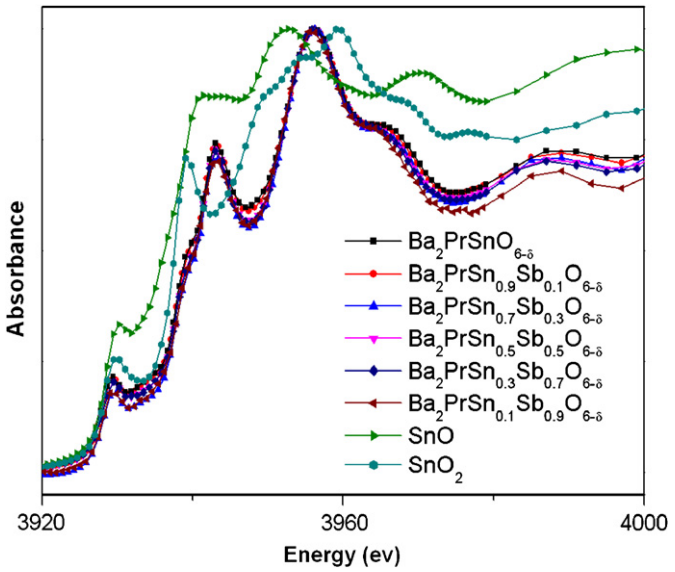

Fig. 8. Sn L_{III}-edges of selected samples in the series $Ba_2PrSn_xSb_{1-x}O_{6-\delta}$ and, the Sn^{2+} and Sn^{4+} standards, SnO and SnO_2.

found for $Ba_2PrSnO_{6-\delta}$ were well established as being typical of Pr^{3+} and Pr^{4+}, respectively, [31–33]. Near-infrared spectra of the Pr oxidation state standards, $Pr_2Sn_2O_7$ and $BaPrO_3$, were found to be similar to those of Ba_2PrSbO_6 and $Ba_2PrSnO_{6-\delta}$, respectively, although the precise energy and intensity of some features varied somewhat. The change in the intensity of these features between the two end-members of the $Ba_2PrSn_xSb_{1-x}O_{6-\delta}$ series appears to be gradual providing a strong indication that the oxidation state changes from Pr^{3+} to Pr^{4+} smoothly across the series.

The near-infrared spectra of Ba_2TbSbO_6 in the 1500–2200 nm region exhibits a number of sharp features, similar to those seen in $Tb_2Sn_2O_7$ and are typical of those of Tb^{3+} [34,35]. Doping with Sn^{4+} results in a rapid loss of these features and the spectra of the $Ba_2TbSnO_{6-\delta}$ lacks any obvious features in this region. $BaTbO_3$ does not have any significant spectral features in this region either, confirming that Tb^{4+} is virtually featureless in the near-infrared region. Evidently, the near-infrared spectra cannot be used to monitor the transition between these two oxides.

Having qualitatively probed the oxidation state of Pr and Tb using near-infrared spectroscopy, XANES was then used to quantify the oxidation state of the various cations present and thereby determine the amount of oxygen vacancies present in the structure. Since Ba cations in metal oxides are almost invariably divalent it was not necessary to investigate Ba using XANES leaving the Sn, Sb, Pr and Tb cations to be examined. Examination of the *L*-edges of Sn and Sb is complicated as a result of all six *L*-edges of these elements occurring in the narrow energy range of 3.9–4.7 keV [36]. This leads to extensive overlap of the Sn L_{II}- and Sb L_{III}-edges, which occur at 4.156 and 4.132 keV, respectively, making analysis of these edges in mixed Sn and Sb compounds very difficult. More importantly, the Sn L_I- and Sb L_{II}-edges (present at 4.465 and 4.380 keV) overlap, although not to such a severe extent. This is particularly problematic in the case of the Sn L_I-edge as this is the edge that would be ideally suited for analysis of the oxidation state of Sn in these compounds. This is because, similar to the Sb L_I-edge, it is the simplest and most sensitive *L*-edge to any change in oxidation state [36–38]. The high sensitivity of the L_I-edge to the oxidation state of Sn and Sb is a result of this transition occurring between the 2*s* and the 5*p* states whose energy depends on the presence or absence of 5*s* electrons.

The problem of using the L_I-edge to determine the oxidation state of Sn was overcome by examining a combination of the Sn

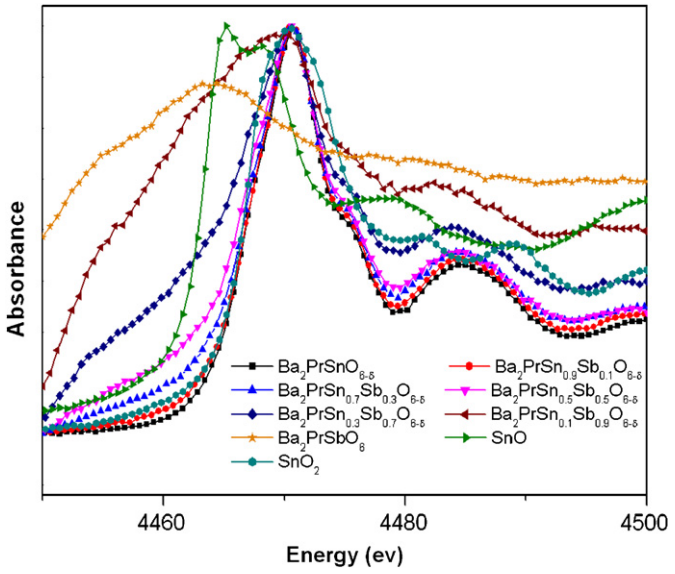

Fig. 9. Sn L_I-edges of selected samples in the series $Ba_2PrSn_xSb_{1-x}O_{6-\delta}$ and, the Sn^{2+} and Sn^{4+} standards, SnO and SnO_2. A rescaled spectrum of Ba_2PrSbO_6 is also included as a reference for the features of the Sb L_{II} post-edge region.

L_I- and L_{III}-edges; the latter being free from any overlap with the Sb *L*-edges. The Sn L_{III}-edge spectra of compounds in the series $Ba_2PrSn_xSb_{1-x}O_{6-\delta}$ and of the three tin doped $Ba_2TbSn_xSb_{1-x}O_{6-\delta}$ ($x = 0.3$, 0.7 and 1.0) samples investigated were very similar suggesting that Sn has the same oxidation state in all of these compounds (see Fig. 8). These spectra were quite different from those of SnO and SnO_2 (which were selected to be used as Sn^{2+} and Sn^{4+} oxidation state standards). The main peak in the Sn L_I absorption edge (also known as a white line) occurred at approximately 4.471 keV in all samples (see Fig. 9). This edge energy is similar to that measured for SnO_2 and no features were observed at the edge energy of SnO. There was, however, another feature at approximately 4.46 keV that increased in intensity with Sb doping. This feature corresponds to a peak in the Sb L_{II} post-edge spectra. Since all Sn L_{III}-edges appear the same and the energy of the Sn L_I-edge does not change with increased tin doping it would seem unlikely that there are any significant

features in the Sn L_I-edge that are being obscured by this interference. It is concluded that the XANES region of the L-edge spectra of Sn demonstrates that Sn adopts a tetravalent oxidation state in these two perovskite series, with no indication of any fraction of Sn^{2+} being present. The disparity between the perovskite spectra and that of SnO_2 indicates a distinctly different co-ordination environment for Sn^{4+} in these two structures. This illustrates the high degree of sensitivity of XANES to co-ordination environment since Sn^{4+} is six-fold co-ordinate in both the perovskite and binary oxides.

The Sn L_I-edge of samples of $Ba_2PrSnO_{6-\delta}$ and $Ba_2TbSnO_{6-\delta}$ that were heated in an atmosphere of 5% H_2 in Ar has an additional shoulder at the low energy side of the edge (see Fig. S4). This feature occurs at 4.464 keV, which is at approximately the same energy as the SnO peak, suggesting that these reduced compounds contain a significant amount of Sn^{2+}. A least-squares fit of the SnO and SnO_2 edges to the spectra of these reduced samples over the range of 4.450–4.480 keV was carried out to determine what fraction of the Sn^{4+} in these samples was reduced to Sn^{2+}. The results from this analysis reveal that the samples of $Ba_2PrSnO_{6-\delta}$ and $Ba_2TbSnO_{6-\delta}$ that were heated up to 800 °C under reducing conditions and then immediately cooled contained approximately 15% Sn^{2+} and 85% Sn^{4+} while the sample of $Ba_2TbSnO_{6-\delta}$ reduced at 800 °C for 24 h had a Sn^{2+} content of about 20%. Evidently reduction of Sn^{4+} in these samples initially occurs rapidly but decreases significantly over time. That some, but not all, of the Sn^{4+} is reduced to Sn^{2+} after 24 h of reduction suggests that thermogravimetric analysis (TGA) of these samples under a reducing atmosphere would not be a valid technique for examining oxygen stoichiometry in these two perovskite series. This is because TGA requires the reduction of all cations in a compound to either the metallic state or to a known lower valency. Indeed attempts to use TGA to analyse the oxygen stoichiometry of $Ba_2PrSnO_{6-\delta}$ and $Ba_2TbSnO_{6-\delta}$ did not yield reliable results. It should be noted that a similar least-squares fit to the XANES region of the as synthesised $Ba_2PrSnO_{6-\delta}$ and $Ba_2TbSnO_{6-\delta}$ compounds does not point to the presence of any Sn^{2+} in these samples confirming that they only contain Sn^{4+}.

Examination of the Sb L_I-edge of compounds in the series $Ba_2PrSn_xSb_{1-x}O_{6-\delta}$ and the Sb containing samples studied in $Ba_2TbSn_xSb_{1-x}O_{6-\delta}$ ($x = 0$, 0.3 and 0.7) indicates that the shape and position of the edge is constant throughout these two series (see Fig. 10). The energy of the white line of the edge in the samples was found to be at 4.705 keV. This is slightly higher than the energy of the edge in the Sb^{5+} standard, Sb_2O_5, and significantly higher than that of the Sb^{3+} standard, Sb_2O_3. This can be interpreted as indicating that the Sb in these two series adopts the pentavalent oxidation state with no Sb^{3+} being present.

Having confirmed that Sn and Sb adopt the tetravalent and pentavalent oxidation states in the as synthesised samples of $Ba_2PrSn_xSb_{1-x}O_{6-\delta}$ and $Ba_2TbSn_xSb_{1-x}O_{6-\delta}$ attention was then turned to quantifying the way in which the oxidation state of Pr and Tb changes throughout the series. In order to achieve this, the Pr and Tb L_{III}-edges were examined because they have higher sensitivity to the oxidation state of these lanthanides. This transition is between the 2*p* and the 5*d* states, the energy of which is particularly dependant on the 4*f* occupancy because of the decrease in effective nuclear charge that occurs with an increased number of 4*f* electrons [39,40].

The energy and shape of the edge region of the Pr L_{III}-edge spectrum of Ba_2PrSbO_6 is very similar to that of the $Pr_2Sn_2O_7$ edge (see Fig. S5). There is, however, some difference in the shape of the post-edge regions of these two spectra, indicating distinct co-ordination environments of Pr in these two samples. As there is no evidence for any features in the edge of Ba_2PrSbO_6 diagnostic of Pr^{4+}, as present in $BaPrO_3$, it can be concluded that only Pr^{3+} is

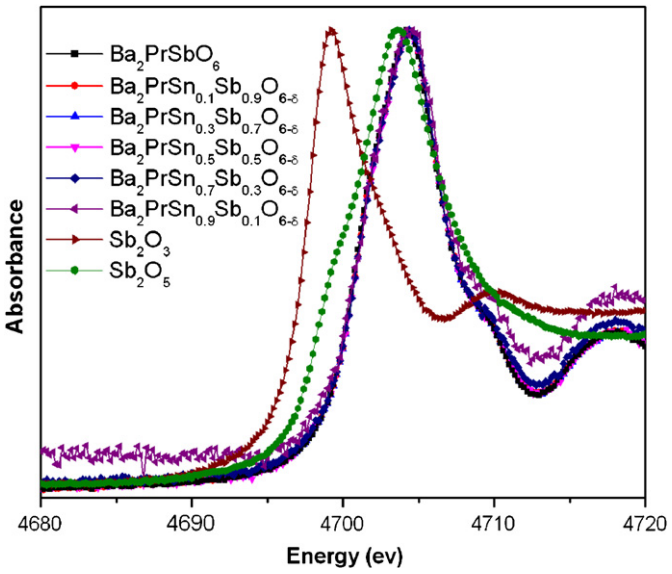

Fig. 10. Sb L_I-edge for selected compounds in the series $Ba_2PrSn_xSb_{1-x}O_{6-\delta}$ and, the Sb^{3+} and Sb^{5+} standards, Sb_2O_3 and Sb_2O_5.

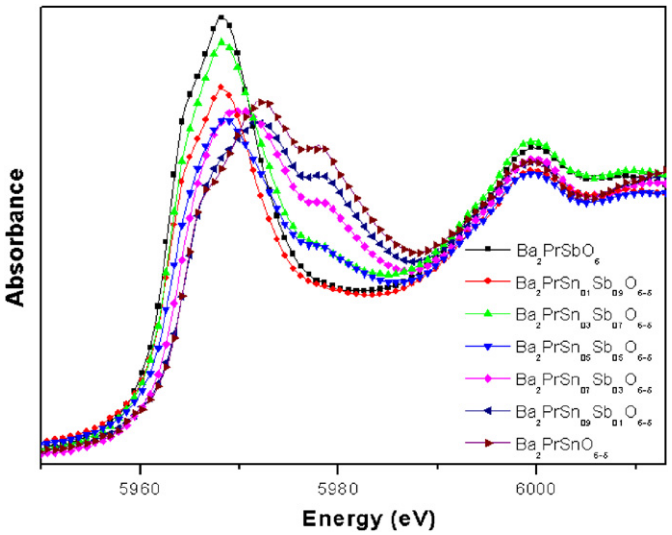

Fig. 11. Pr L_{III}-edge spectra of selected compounds in the series $Ba_2PrSn_xSb_{1-x}O_{6-\delta}$ indicating the change in the energy and shape of the edge between 5960 and 5985 eV with increasing x.

present in this compound. The Pr L_{III}-edge in $Ba_2PrSnO_{6-\delta}$, on the other hand, is very similar to that measured for $BaPrO_3$, with the white line associated with this edge occurring at 5.972 keV (see Fig. S5).

The Pr L_{III}-edges of the intermediate compounds in the series $Ba_2PrSn_xSb_{1-x}O_{6-\delta}$ indicate that as x increases the Pr^{3+}-like features of Ba_2PrSbO_6 gradually decrease in intensity while the Pr^{4+}-like features of $Ba_2PrSnO_{6-\delta}$ slowly increase (see Fig. 11). Principal component analysis (PCA) of the intermediate samples in the series was carried out over the energy range of 5.902–6.200 keV, using the PCA program belonging to the EXAFSPAK suite [41]. This analysis revealed that there were only two significant components in the spectra of all the intermediate members of the series. Target transformation analysis [41] demonstrated that these two components were well matched by the Ba_2PrSbO_6 and $Ba_2PrSnO_{6-\delta}$ end members of the series. The end members were better fits for the target transformation than

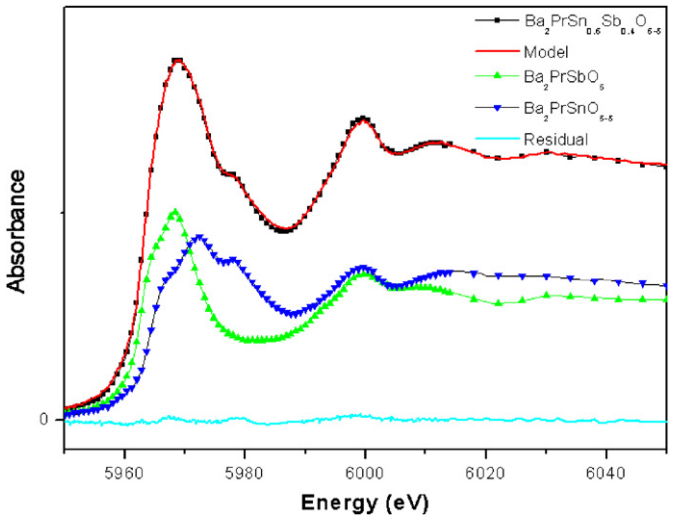

Fig. 12. Plot of the L_{III}-edge of $Ba_2PrSn_{0.6}Sb_{0.4}O_{6-\delta}$ and the model spectrum fitted to it, including the Ba_2PrSbO_6 and $Ba_2PrSnO_{6-\delta}$ components of the fit.

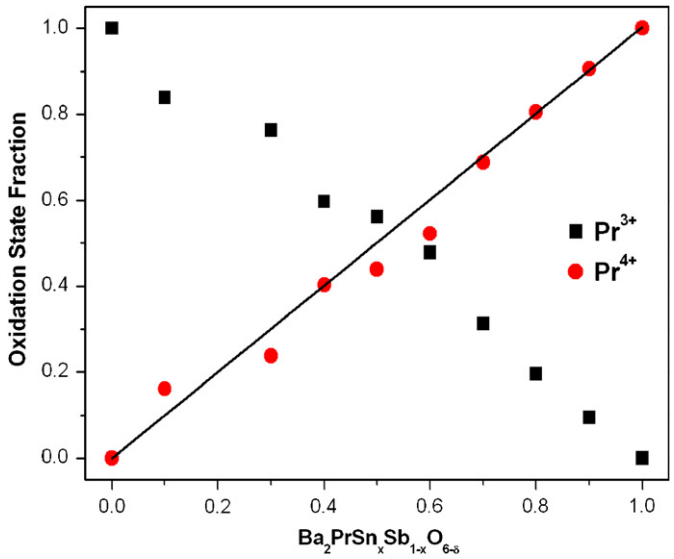

Fig. 13. Plot of the oxidation state fraction of Pr^{3+} and Pr^{4+} in each compound examined in the $Ba_2PrSn_xSb_{1-x}O_{6-\delta}$ series. The black line indicates the amount of Pr^{4+} required at each composition for there to be no oxygen vacancies present and is drawn as a guide to the eye. The $x = 0.2$ sample was not investigated due to experimental constraints.

the $Pr_2Sn_2O_7$ and $BaPrO_3$ standards principally because the different co-ordination environment of Pr^{3+} in $Pr_2Sn_2O_7$ means that shape of the post-edge region of $Pr_2Sn_2O_7$ is significantly different from that of the Pr^{3+} in the perovskite series. While Pr in the perovskite samples studied occupies an octahedral site (six co-ordinate), it is eight co-ordinate in the $Pr_2Sn_2O_7$ standard and the differences between the Pr L_{III}-edge spectra of $Pr_2Sn_2O_7$ and Ba_2PrSbO_6 highlight the sensitivity of XANES to different bonding environments. Unfortunately, there were no suitable perovskite standards in which the Ln^{3+} cations adopt an octahedral site.

All the techniques used in this work to probe the oxidation state of Pr in Ba_2PrSbO_6 and $Ba_2PrSnO_{6-\delta}$ indicate that it is purely trivalent and tetravalent, respectively, in these two samples. These two compounds were utilised as Pr^{3+} and Pr^{4+} standards and thereby the oxidation state of Pr in the intermediate members of the $Ba_2PrSn_xSb_{1-x}O_{6-\delta}$ series was accurately determined. This was done by carrying out a least-squares refinement of the Pr L_{III}-edge spectra of the two end-member compounds against the spectra for each of the individual intermediate compounds over the energy range of the 5.950–6.050 keV using the DATFIT program (see Fig. 12 for an example of the quality of the fits obtained) [27,41]. This analysis found that the ratio of Pr^{3+} to Pr^{4+} gradually changes across the series with the amount of Pr^{4+} increasing with increasing Sn^{4+} concentration (see Fig. 13).

Since it has been established that Sn and Sb cations adopt the tetravalent and pentavalent oxidation states and assuming Ba always adopts the divalent state in perovskite-type materials, the amount of oxygen vacancies in each compound could then be determined from the amount of Pr^{3+} and Pr^{4+} found to be present via the least-squares analysis. As can be seen in Table 5, there is not a significant amount of oxygen vacancies in any member of the $Ba_2PrSn_xSb_{1-x}O_{6-\delta}$ series, with the oxidation state change of Pr^{3+} to Pr^{4+} fully compensating for the charge loss of Sn^{4+} substituting for Sb^{5+}. It should be noted that a similar least-squares analysis of the H_2 reduced sample of $Ba_2PrSnO_{6-\delta}$ found that this sample contains only Pr^{3+}. The energy of the Pr L_{III}-edge is slightly lower in the H_2 reduced sample than found for Ba_2PrSbO_6 suggesting that the presence of oxygen vacancies, or Sn^{4+} instead of Sb^{5+} in neighbouring octahedra, has some small effect on the energy of the edge (see Fig. S5).

The Tb L_{III}-edge of Ba_2TbSbO_6 has a white line at approximately 7.512 keV very close to that of the Tb^{3+} standard, $Tb_2Sn_2O_7$, strongly suggesting that Tb in this compound is trivalent (see Fig. S6). Similar to the Pr L_{III}-edges of $Pr_2Sn_2O_7$ and Ba_2PrSbO_6, the post-edge region of the two terbium edges is significantly different, an observation that can be attributed to the different environment of Tb in the pyrochlore and perovskite structures. Since there is no evidence for any feature in the L_{III}-edge of Ba_2TbSbO_6 at the energy of the Tb^{4+} standard ($BaTbO_3$), it can be concluded that all the Tb in this compound is trivalent. On the other hand, the L_{III}-edge spectra of $Ba_2TbSnO_{6-\delta}$ has both a similar shape and position to that of $BaTbO_3$ indicating that all Tb in this compound is tetravalent (see Fig. S6). This is consistent with the majority of structural data and near-infrared spectroscopy. Evidently, the neutron diffraction analysis has overestimated the number of oxygen vacancies, and hence Tb^{3+} content, in $Ba_2TbSnO_{6-\delta}$. As stated previously this error could arise from cross-correlation between the site occupancy and atomic displacement parameters.

Qualitatively examining the XANES region of the spectra of the intermediate compounds in the $Ba_2TbSn_xSb_{1-x}O_{6-\delta}$ series shows that as x increases the Tb^{3+}-like features of Ba_2TbSbO_6 lose intensity while the Tb^{4+} like features in $Ba_2TbSnO_{6-\delta}$ increase in

Table 5
Oxygen stoichiometry as determined by the least-squares fit of the Pr and Tb L_{III}-edges for perovskites in the series $Ba_2LnSn_xSb_{1-x}O_{6-\delta}$ (Ln = Pr or Tb)

$Ba_2LnSn_xSb_{1-x}O_{6-\delta}$	Oxygen stoichiometry	
x	Pr	Tb
0	6.00(1)	6.00(1)
0.1	6.03(2)	5.95(1)
0.2	N/A	5.95(1)
0.3	5.97(1)	5.95(1)
0.4	6.00(2)	5.96(1)
0.5	5.97(2)	5.97(1)
0.6	5.96(1)	5.97(1)
0.7	5.99(1)	5.97(1)
0.8	6.00(1)	5.99(1)
0.9	6.00(1)	5.99(1)
1.0	6.00(1)	6.00(1)

intensity (see Fig. 14). Having established that the Tb in Ba_2TbSbO_6 is all trivalent, while $Ba_2TbSnO_{6-\delta}$ contains only Tb^{4+} the intermediate compounds in the series $Ba_2TbSn_xSb_{1-x}O_{6-\delta}$ were analysed in a similar manner to the analogous Pr series. PCA of the 7.425–7.800 keV region of the spectra of the intermediate compounds indicated that they consist of only two common components, which target transformation analysis confirmed were good matches to the spectra of Ba_2TbSbO_6 and $Ba_2TbSnO_{6-\delta}$. A least-squares analysis was then used to fit the region 7.475–7.675 keV, using the end-member spectra as components, to determine what fraction of Tb^{3+} and Tb^{4+} was present.

The least-squares analysis of the intermediate compounds shows that the rate at which Tb^{3+} changes to Tb^{4+} as Sn^{4+} substitutes for Sb^{5+} is not sufficient in the samples with a small amount of Sn^{4+} to totally prevent the formation of oxygen vacancies. In the series $Ba_2TbSn_xSb_{1-x}O_{6-\delta}$, the $x = 0.1$–0.3 samples were found to have $\delta \approx 0.05$ (see Fig. 15 for the oxidation state fraction of Tb and Table 5 for the amount of oxygen vacancy in each compound). As the amount of Sn^{4+} doping is increased beyond $x = 0.3$ the number of oxygen vacancies present appears to gradually decrease achieving a fully stoichiometric perovskite with respect to oxygen for $Ba_2TbSnO_{6-\delta}$. This contrasts with the results for $Ba_2PrSn_xSb_{1-x}O_{6-\delta}$, where there was no consistent evidence for oxygen vacancies. A least-squares fit of the Tb L_{III}-edge spectra for a reduced sample of $Ba_2TbSn_xSb_{1-x}O_{6-\delta}$, suggested that all the Tb^{4+} had been reduced to Tb^{3+} upon heating to 800 °C in 5% H_2 in Ar (see Fig. S6 for XANES spectra).

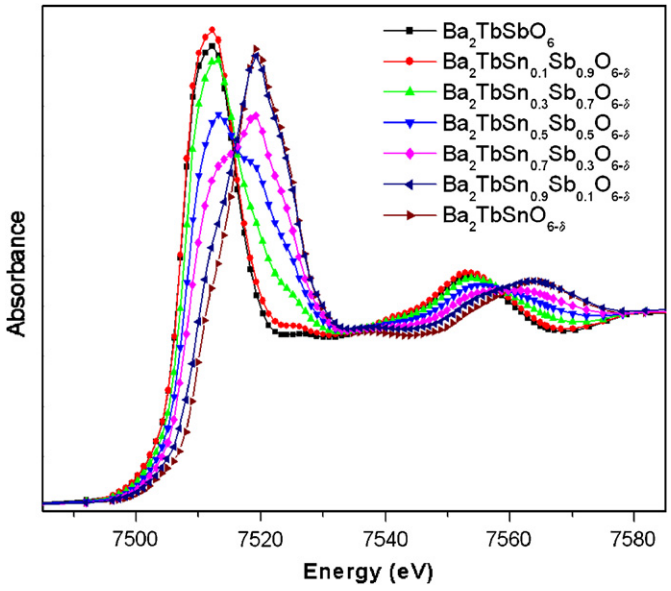

Fig. 14. Tb L_{III}-edge spectra of selected compounds in the series $Ba_2TbSn_xSb_{1-x}O_{6-\delta}$ indicating the change in the energy and shape of the edge between 7485 and 7585 eV with increasing x.

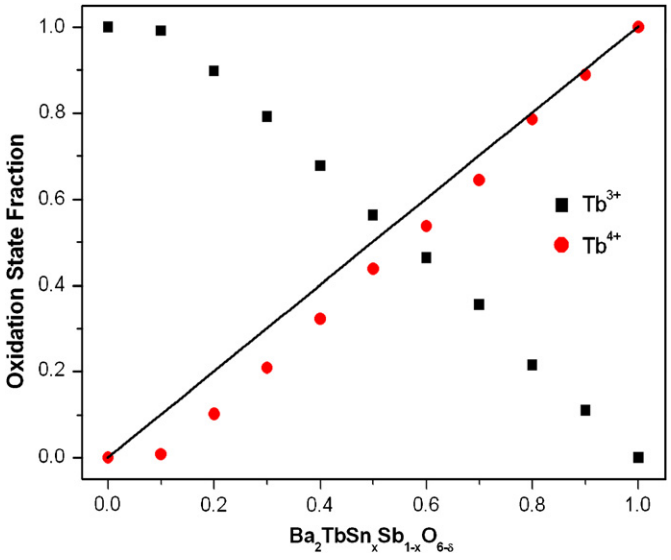

Fig. 15. Plot of the oxidation state fraction of Tb^{3+} and Tb^{4+} in each compound examined in the $Ba_2TbSn_xSb_{1-x}O_{6-\delta}$ series. The black line depicts the amount of Tb^{4+} required at each composition for there to be no oxygen vacancies present and is drawn as a guide to the eye.

4. Conclusion

The compounds in the series $Ba_2LnSn_xSb_{1-x}O_{6-\delta}$ (Ln = Pr and Tb) have been synthesised and structurally characterised using synchrotron X-ray and neutron diffraction. The two end-member compounds of the $Ba_2PrSn_xSb_{1-x}O_{6-\delta}$ series, Ba_2PrSbO_6 and $Ba_2PrSnO_{6-\delta}$ were found to adopt $R\bar{3}$ and $R\bar{3}c$ symmetries, respectively, with the difference in structure between these compounds being caused by the loss of B-site cation ordering in $Ba_2PrSnO_{6-\delta}$. This was found to be caused by the oxidation state change of Pr from Pr^{3+} in the former to Pr^{4+} in the latter. Similarly, Ba_2TbSbO_6 and $Ba_2TbSnO_{6-\delta}$ were found to both adopt cubic symmetry with B-site cation ordering present in the former but absent in the latter due to the oxidation state change of Tb from Tb^{3+} to Tb^{4+}.

It was found that $Ba_2PrSn_xSb_{1-x}O_{6-\delta}$ features a large two-phase region of $I2/m$ monoclinic and $R\bar{3}c$ rhombohedral symmetries over the composition range of $x = 0.3$–0.9. This is likely to be due to the segregation of Pr^{3+} and Pr^{4+} into these two separate structures. In contrast, all intermediate $Ba_2TbSn_xSb_{1-x}O_{6-\delta}$ samples were found to be single-phase cubic structures with B-site cation disordering increasing gradually with increasing x until a phase transition occurs from $Fm\bar{3}m$ to $Pm\bar{3}m$ symmetries between $x = 0.8$ and 0.9. L_{III}-edge XANES and near-infrared spectroscopy show that the oxidation state change of Pr and Tb, from the trivalent to tetravalent state, occurs gradually with increasing x. Least-squares fitting of the Pr L_{III}-edge spectra indicates that Pr^{3+} undergoes an oxidation state change to Pr^{4+} concomitant with increased Sn^{4+} doping so there is not a significant number of oxygen vacancies present. On the other hand in the Tb series, it was shown that the rate of conversion of Tb^{3+} to Tb^{4+} was too slow for small amounts of Sn^{4+} doping to eliminate the presence of oxygen vacancies leading to a maximum oxygen deficiency of $\delta = 0.05$.

Acknowledgments

This work was partially supported by the Australian Research Council. The neutron diffraction work has been supported by the Australian Institute of Nuclear Science and Engineering (AINSE) through the provision of an AINSE Postgraduate Award. The work performed at the Australian National Beamline Facility and at the NSRRC was supported by the Australian Synchrotron Research Program under the Major National Research Facilities program. The synchrotron X-ray diffraction was performed with the help of Dr. James Hester.

Appendix A. Supplementary data

Supplementary data associated with this article can be found in the online version at doi:10.1016/j.jssc.2008.07.007.

References

[1] R.H. Mitchell, Perovskites Modern and Ancient, Almaz Press Inc., Ontario, 2002.
[2] V.V. Kharton, F.M.B. Marques, A. Atkinson, Solid State Ionics 174 (2004) 135–149.
[3] J.B. Goodenough, Rep. Prog. Phys. 67 (2004) 1915–1993.
[4] S.J. Skinner, Int. J. Inorg. Mater. 3 (2001) 113–121.
[5] T. Ishihara, H. Matsuda, Y. Takita, J. Am. Chem. Soc. 116 (1994) 3801–3803.
[6] N. Bonanos, K.S. Knight, B. Ellis, Solid State Ionics 79 (1995) 161–170.
[7] P. Murugaraj, K.D. Kreuer, T. He, T. Schober, J. Maier, Solid State Ionics 98 (1997) 1–6.
[8] K.D. Kreuer, Solid State Ionics 97 (1997) 1–15.
[9] Q. Zhou, B.J. Kennedy, J. Solid State Chem. 178 (2005) 3589–3594.
[10] L. Li, B.J. Kennedy, J. Solid State Chem. 177 (2004) 3290–3300.
[11] R.D. Shannon, Acta Crystallogr. A 32 (1976) 751–767.
[12] J. Kurian, J. Koshy, P.R.S. Wariar, Y.P. Yadava, A.D. Damodaran, J. Solid State Chem. 116 (1995) 193–198.
[13] K.V. Paulose, J. Koshy, A.D. Damodaran, Supercond. Sci. Technol. 5 (1992) 31–33.
[14] C.J. Howard, B.J. Kennedy, P.M. Woodward, Acta Crystallogr. B 59 (2003) 463–471.
[15] P.J. Saines, B.J. Kennedy, M.M. Elcombe, J. Solid State Chem. 180 (2007) 401–409.
[16] W.T. Fu, D.J.W. IJdo, J. Solid State Chem. 178 (2005) 2363–2367.
[17] T.M. Sabine, B.J. Kennedy, R.F. Garrett, G.J. Foran, D.J. Cookson, J. Appl. Crystallogr. 28 (1995) 513–517.
[18] C.J. Howard, C.J. Ball, R.L. Davis, M.M. Elcombe, Aust. J. Phys. 36 (1983) 507–518.
[19] B.A. Hunter, C.J. Howard, A Computer Program for Rietveld Analysis of X-ray and Neutron Powder Diffraction Patterns, Lucas Heights Laboratories, 1998.
[20] R.J. Hill, J. Appl. Crystallogr. 25 (1992) 589–610.
[21] H.G. Scott, J. Appl. Crystallogr. 16 (1983) 159–163.
[22] L.-Y. Jang, S.-H. Chang, BL15B DCM Tender X-ray Beamline 〈http://140.110.203.42/bldoc/15BDCM1-9.htm〉 (27/09/2007).
[23] T.-E. Dann, S.-C. Chung, L.-J. Huang, J.-M. Juang, C.-I. Chen, K.-L. Tsang, J. Synchrotron Radiat. 5 (1998) 664–666.
[24] B.J. Kennedy, B.A. Hunter, C.J. Howard, J. Solid State Chem. 130 (1997) 58–65.
[25] M. Yoshimura, T. Nakamura, T. Sata, Bull. Tokyo Inst. Technol. 120 (1974) 13–27.
[26] Y. Hinatsu, J. Alloy. Compds. 193 (1993) 113–115.
[27] G.N. George, I.J. Pickering, EXAFSPAK: A Suite of Computer Programs for Analysis of X-ray Absorption Spectra, Stanford Synchrotron Radiation Laboratory, 2000.
[28] P.J. Ellis, H.C. Freeman, J. Synchrotron Radiat. 2 (1995) 190–195.
[29] V. Ting, Y. Liu, R.L. Withers, L. Norén, M. James, J.D. Fitz Gerald, J. Solid State Chem. 179 (2006) 551–562.
[30] V.F. Sears, Neutron News 3 (1992) 26–37.
[31] D.A. Pawlak, T. Lukasiewicz, M.A. Carpenter, M. Malinowski, R. Diduszko, J. Kisielewski, J. Cryst. Growth 282 (2005) 260–269.
[32] D. Pawlak, Z. Frukacz, Z. Mierczyk, A. Suchocki, J. Zachara, J. Alloy. Compds. 275–277 (1998) 361–364.
[33] W.A. Pisarski, J. Pisarska, G. Dominiak-Dzik, W. Ryba-Romanowski, J. Phys.: Condens. Matter 16 (2004) 6171–6184.
[34] L. Ning, C.S.K. Mak, P.A. Tanner, Phys. Rev. B: Condens. Matter 72 (2005) 085127.
[35] V.F. Zolin, J. Alloy. Compds. 380 (2004) 101–106.
[36] J. Rockenberger, U. Zum Felde, M. Tischer, L. Tröger, M. Haase, H. Weller, J. Chem. Phys. 112 (2000) 4296–4304.
[37] J.M.M. Millet, M. Baca, A. Pigamo, D. Vitry, W. Ueda, J.L. Dubois, Appl. Catal. A-—Gen. 244 (2003) 359–370.
[38] Z. Liu, K. Handa, K. Kaibuchi, Y. Tanaka, J. Kawai, J. Electron Spectrosc. Relat. Phenom. 135 (2004) 155–158.
[39] H. Arashi, S. Shin, H. Miura, A. Nakashima, M. Ishigame, Solid State Ionics 35 (1989) 323–327.
[40] T.W. Capehart, R.K. Mishra, J.F. Herbst, J. Appl. Phys. 72 (1992) 676–679.
[41] G.N. George, I.J. Pickering, Principal Component Analysis and Target Transformation Using EXAFSPAK: Notes for Version 0.1, Stanford Synchrotron Radiation Laboratory, 2002.